WILEY-VCH

DOI: 10.1002/ aenm.201701678
Article type: Full Paper

From Recombination Dynamics to Device Performance: Quantifying the Efficiency of Exciton Dissociation, Charge Separation, and Extraction in Bulk Heterojunction Solar Cells with Fluorine-Substituted Polymer Donors

Julien Gorenflot, Andreas Paulke, Fortunato Piersimoni, Jannic Wolf, Zhipeng Kan, Federico Cruciani, Abdulrahman El Labban, Dieter Neher, Pierre M. Beaujuge, Frédéric Laquai**

Dr. J. Gorenflot, Dr. Z. Kan, Dr. A. El Labban, Prof. P. M. Beaujuge, Prof. F. Laquai
King Abdullah University of Science and Technology (KAUST), KAUST Solar Center (KSC), Physical Sciences and Engineering Division (PSE), Material Science and Engineering Program (MSE), Thuwal, 23955-6900, Kingdom of Saudi Arabia
E-mail: julien.gorenflot@kaust.edu.sa; frederic.laquai@kaust.edu.sa

Dr. J. Wolf, F. Cruciani
King Abdullah University of Science and Technology (KAUST), KAUST Solar Center (KSC), Chemical Sciences Program, Thuwal, 23955-6900, Kingdom of Saudi Arabia

A. Paulke, Dr. F. Piersimoni, Prof. D. Neher
Institut für Physik und Astronomie, Physik weicher Materie, University of Potsdam, Karl-Liebknecht-Straße 24−25, 14476 Potsdam-Golm, Germany

Keywords: Bulk heterojunction, charge generation yield, charge recombination yield, polymer solar cells, transient absorption spectroscopy

Abstract

An original set of experimental and modeling tools is used to quantify the yield of each of the physical processes leading to photocurrent generation in organic bulk heterojunction solar cells, enabling evaluation of materials and processing condition beyond the simple comparison of device performances. Transient absorption (TA) spectroscopy, 'the' technique to monitor all intermediate states over the entire relevant timescale, is combined with time-delayed collection field (TDCF) experiments, transfer matrix simulations, spectral deconvolution, and parametrization of the charge carrier recombination by a two-pool model, allowing quantification of densities of excitons and charges and extrapolation of their kinetics to device-relevant conditions. Photon absorption, charge transfer, charge separation, and charge extraction are all quantified for two recently developed wide-bandgap donor polymers: poly(4,8-bis((2-ethylhexyl)oxy)benzo[1,2-*b*:4,5-*b'*]dithiophene-3,4-difluorothiophene) (PBDT[2F]T) and its non-fluorinated counterpart (PBDT[2H]T) combined with $PC_{71}BM$ in bulk heterojunctions (BHJ). The product of these yields is shown to agree well with the devices' EQE. This methodology elucidates in the specific case studied here the origin of improved photocurrents obtained when using PBDT[2F]T instead of PBDT[2H]T as well as upon using solvent additives. Furthermore, a higher CT-state energy is shown to lead to significantly lower energy losses (resulting in higher V_{OC}) during charge generation compared to P3HT:PCBM.

1. Introduction

Cost-effective production, solution-processability, non-toxicity, and the possibility to tailor the electronic and optical properties of polymers towards specific requirements: conjugated polymers possess a unique set of advantages, which make them interesting for solar cell applications. However, the wide-spread adoption of polymers as photoactive materials in solar cells still faces a number of challenges, including photoactive layer degradation effects due to (photo)stability limitations, and power conversion efficiencies (PCE) lagging behind those of other technologies such as inorganic systems,[1] and organic-inorganic hybrid perovskites.[2,3] Yet, tremendous research efforts in the past years have propelled the PCE beyond 12% with nonfullerene acceptors,[4] while maximum efficiencies of over 20% have been predicted for fully optimized material systems and device structures.[5]

To achieve this potential, conjugated polymers can take advantage of the sheer infinite possibilities that molecular engineering offers to tailor their optical, electronic, morphological, and photophysical properties. In parallel, a broad range of processing parameters such as various solvents, additives, post-processing thermal and solvent vapor annealing approaches can be used to further adjust some of those parameters. And yet, this tremendous potential will remain a myth without the tools to evaluate the effect of those synthetic and processing

approaches on photocurrent generation and identify, within this virtual infinity of material systems, those that will be able to solve the challenges faced by the OPV field. The complexity of this evaluation originates from the multistep nature of photocurrent generation in OPV which involves: (1) photon absorption generating a bound electron-hole pair (exciton), (2) (ultra)fast charge transfer across or diffusion-limited exciton dissociation at the heterojunction, (3) charge separation, *i.e.* escape of charges from their mutual coulomb attraction potential, and (4) charge transport to the device electrodes followed by extraction. Consequently, the external quantum efficiency (*EQE*) of devices is the product of the individual efficiencies of each of the aforementioned steps, precisely: $EQE = \varphi_{abs} \times \varphi_{ct} \times \varphi_{sep} \times \varphi_{extr}$, where φ_{abs}, φ_{ct}, φ_{sep} and φ_{extr} are the yields of photon absorption, charge transfer, charge separation, and charge carrier extraction, respectively. In order to further progress, the OPV field is in great need of new approaches able to quantitatively evaluate the effects of molecular structures and processing conditions on each of those steps, and thereby to find the best way to combine them.

In this study, we present a methodology to determine each of the intermediate yields and thus to accurately pinpoint the strengths and weaknesses of material systems, which often remain hidden behind the simple device figures of merit. Our method is based on transient absorption (TA) which is, to the best of our knowledge, the only experimental method able to monitor excited states as different as neutral excitons (and sometimes triplets), spatially-separated

charges (SSC), and bound pairs of charges (BCP) in the required time range spanning from sub-picosecond (exciton diffusion) to hundreds of microseconds (free charge recombination competing with extraction). Such studies have already been used in the past to qualitatively identify the loss channels competing with the different steps of photocurrent generation.[6-10] However, three major obstacles often prevent researchers from obtaining quantitative information: firstly, excited states in disordered material systems, to which polymer:fullerene blends belong, exhibit broad and largely overlapping absorption bands. Spectral regions where only one state absorbs are rare, if they exist at all, often leading to kinetics with substantial noise levels that are difficult to analyze. Secondly, the optical signal (for instance change in transmission) is difficult to translate into an accurate density of excited states, because the proportionality factor, namely the absorption cross-section σ, is generally unknown. Lastly, the pump pulse photon density used in TA experiments is typically orders of magnitude higher than that for practical solar cell operating conditions, an experimental constraint owing to the limited signal-to-noise ratio, which may lead to dynamics that differ substantially from those occurring under practical device operation conditions.

To overcome these obstacles, we used a combination of optical and electro-optical spectroscopy techniques and advanced data analysis and modeling tools. Namely, the spectral overlap of excited states is disentangled by obtaining reference spectra of excitons and charges

and solving the TA spectra as a time dependent linear combination of those two contributions; the charge carrier absorption cross section is obtained by comparing the TA data to charge densities extracted from time-delayed collection field (TDCF) experiments carried out in equivalent illumination, and the mismatch between TA experiments and device operation conditions is resolved by parametrizing the carrier decay observed in TA using a two-pool model which yields the required recombination parameters to extrapolate the decays to lower illumination densities such as one sun.

2. Results and Discussion

2.1. Material systems and methodology

For our case study, we chose two recently developed, structurally analogous wide-bandgap conjugated polymers – namely poly(4,8-bis((2-ethylhexyl)oxy)benzo[1,2-*b*:4,5-*b'*]-3,4-difluorothiophene) (PBDT[2F]T) and its non-fluorinated counterpart poly(4,8-bis((2-ethylhexyl)oxy)benzo[1,2-*b*:4,5-*b'*]dithiophene-3,4-thiophene) (PBDT[2H]T) – whose molecular structures are depicted in **Figure 1**. The polymer syntheses, film morphologies, and BHJ solar cell performance figures were described in a recent, separate study,[11] as well as the intrinsic packing and transport properties of the neat polymers.[12] In short, BHJ solar cells made with PBDT[2F]T and $PC_{71}BM$ can yield PCEs as high as 7% with an average over 6% (detailed figures of merit can be found in ref. [11] and in **Table S1**) and thus largely outperform BHJ devices made with, for instance, the regioregular polymer donor poly(3-hexylthiophene) (RR-P3HT) and $PC_{61}BM$, despite an onset of absorption at higher photon energy (shorter wavelength).

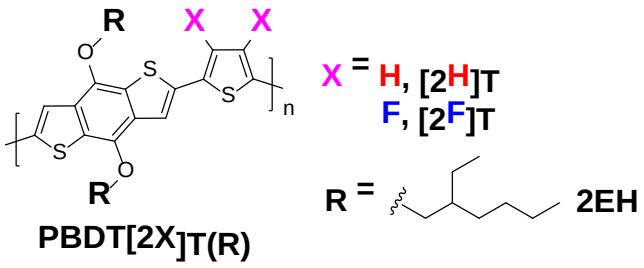

Figure 1. Chemical structures of the polymer donors PBDT[2F]T and PBDT[2H]T investigated in this case study. The polymer syntheses, film morphologies, and BHJ solar cell performance figures were described in a recent, separate study.[11]

The determination of the efficiency of each of the successive steps of photocurrent generation helps to understand the photophysics that determine the device performance of each system. They are the subjects of this study: (i) the light absorption yield φ_{abs} is determined from steady-state absorption measurements combined with transfer matrix simulations of light confinement in the device structure (including refractive indexes determined by ellipsometry). (ii) The charge generation (or charge transfer) yield φ_{CT} is determined from the quantification of the time-dependent charge density profile obtained by deconvoluting the contributions of charges and excitons to transient absorption spectra and comparing the optical signal amplitudes to charge densities determined by time-delayed collection field experiments under equivalent excitation conditions. (iii) The charge separation yield φ_{sep} is determined by parametrization of the charge density decay using a two-pool recombination model, which enables to extract the fractions of spatially-separated charges

(SSC) and coulombically-bound charge pairs (BCP). (iv) The charge extraction yield φ_{extr} is determined by extrapolation of the parametrized decays to conditions relevant for device operation and evaluation of the density of charges remaining at the extraction time. **Figure 2** shows a simplified flowchart representing the steps (ii), (iii) and (iv) of our methodology, a more detailed flowchart can be found in the Support Information (**Figure S1**). We complete the study by the determination of the Charge Transfer state (CT) energy from CT absorption and emission spectra, which reveals the energetic cost of photocurrent generation.

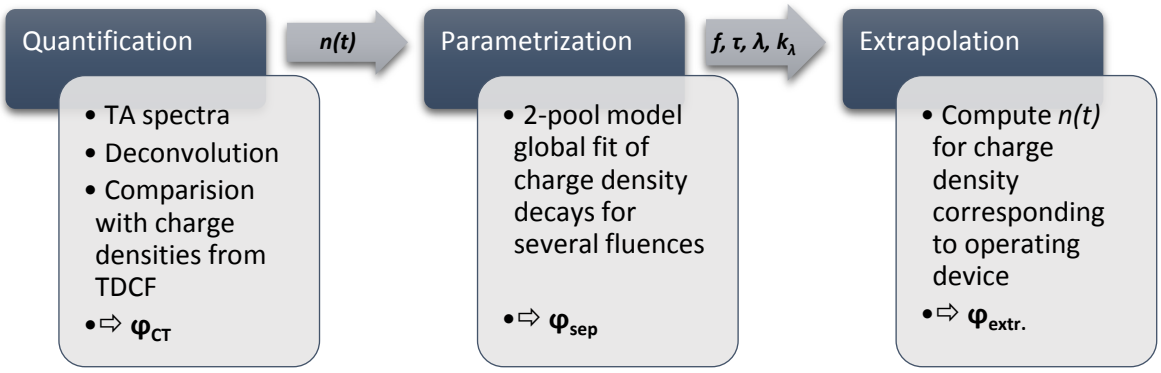

Figure 2. Simplified flowchart for the determination of the charge transfer, charge separation and charge extraction yields. *n(t)* represent the time dependent charge density, *f* the fraction of separated charges, τ the lifetime of bound charge pairs, and k_λ the empirical coefficient for non geminate recombination of apparent order $\lambda+1$.

Applied to the case of PBDT[2X]T blends, our methodology is able to explain the following observations: (i) the higher performance of PBDT[2F]T:$PC_{71}BM$-based BHJ solar cells (avg.

6.8 %) compared with devices based on its non-fluorinated polymer counterpart PBDT[2H]T (avg. 2.3 %), specifically a twofold increase in short-circuit current, a 10% increase of the fill factor and a 0.1 V increase in V_{OC} , (ii) the effect of morphological changes on the short-circuit current and device efficiency when using chloronaphthalene (CN) as a solvent additive (solvent: chlorobenzene, CB), and (iii) the largely improved open-circuit voltage (0.9 V) of PBDT[2F]T:$PC_{71}BM$-based BHJ devices compared with that of the benchmark RR-P3HT:$PC_{61}BM$ (0.6 V). In the following sections, we abbreviate the polymer donors as [2F]T, [2H]T, and [2X]T (with X= H or F) when referring to the fluorinated, non-fluorinated, or either of the polymers, respectively.

2.2. Steady-state absorption

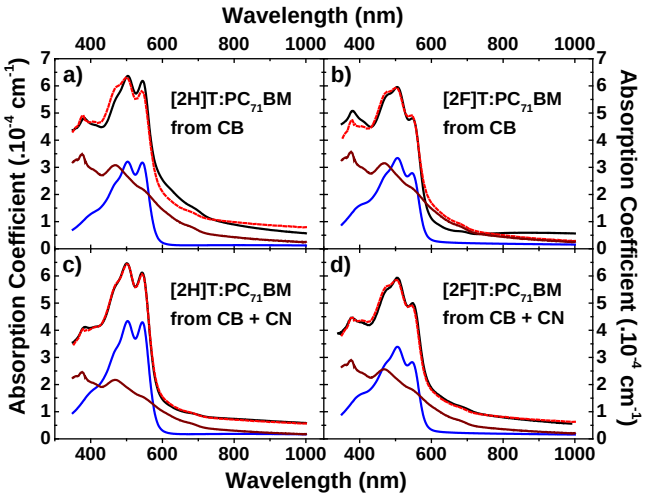

Figure 3. Wavelength dependence of the decadic absorption coefficient for the four thin film [2X]T:$PC_{71}BM$ blends spin-cast on quartz substrates according to device optimal conditions: 1:1.5 (wt./wt.) [2X]T:$PC_{71}BM$ ratio from 20 mg mL^{-1} chlorobenzene (CB) solutions (a) (b) without additive, (c) (d) with optimal 5% (v/v) 1-chloronaphthalene (CN) solvent additive. The black line depicts the coefficient extracted from UV-Vis-NIR absorption spectroscopy, the red dashed line the absorption spectrum reconstructed from the sum of the neat components, namely $PC_{71}BM$ (brown line) and neat polymer (blue line).

All four investigated polymer:fullerene blends exhibit high absorption coefficients of 4-6×10^{-4} cm^{-1} and very similar absorption spectra (see **Figure 3**). Blending the polymers with $PC_{71}BM$ does not appear to modify their packing, as no obvious spectral changes in the polymer absorption are observed in blends when comparing the spectra of the neat polymer films. In fact, the blends' absorption spectra can be reconstructed by a superposition of the absorption spectra of the neat materials. However, the relative contribution of the polymers appears to be lower in the case of blends prepared without the solvent additive, while the same

[2X]T:$PC_{71}BM$ composition (1:1.5 w/w) was used to prepare the films. This could be due to the larger extent of fullerene aggregation induced by the use of CN as solvent additive,[13,14] which implies a lower density of donor:acceptor interface, leading to the formation of less ground state interfacial charge-transfer states. Indeed, these states were recently found to bleach the low-energy part of the absorption spectra of polymer:fullerene blends, corresponding to the region of polymer absorption in the present case study.[15] Alternatively, the CN-induced fullerene aggregation, possibly already present in solution, could lead to differences in the solution-to-film solidification during spin-coating, in turn leading to an actual difference in the films polymer:fullerene ratio as suggested by the higher dielectric constant measured by ellipsometry – close to that of neat fullerene – for the films processed without CN (see **Table S2**). We also note that the onset of absorption of [2X]T:$PC_{71}BM$ occurs at a slightly higher energy than that of RR-P3HT:$PC_{61}BM$, which makes [2X]T:$PC_{71}BM$ blends some of the most promising photovoltaic systems for organic hetero-tandem device configurations in combination with complementary, lower-bandgap materials.

2.3. Charge generation

In earlier work, we showed that photoluminescence (PL) quenching in blends of [2X]T:PC71BM is efficient, with over 90% quenching reported for all 4 blends.[11] To

investigate whether this PL quenching is associated to charge generation, we performed Vis-NIR transient absorption pump-probe spectroscopy covering a dynamic range from sub-ps to microseconds in [2X]T:PC71BM blends. In this section, we first identify the states contributing to the transient spectra and qualitatively examine their evolution, then we deconvolute their contribution to obtain charge density profiles (which are unit-less at first), and finally we compare the optical signal from charges at 10 ns to the amount of charges extracted by time delayed collection field experiments for the same delay time which allows to quantify the charge density profiles or equivalently to calculate the absorption cross section of charges. This section is completed by studying the field dependence of charge generation.

2.3.1. Transient absorption spectra

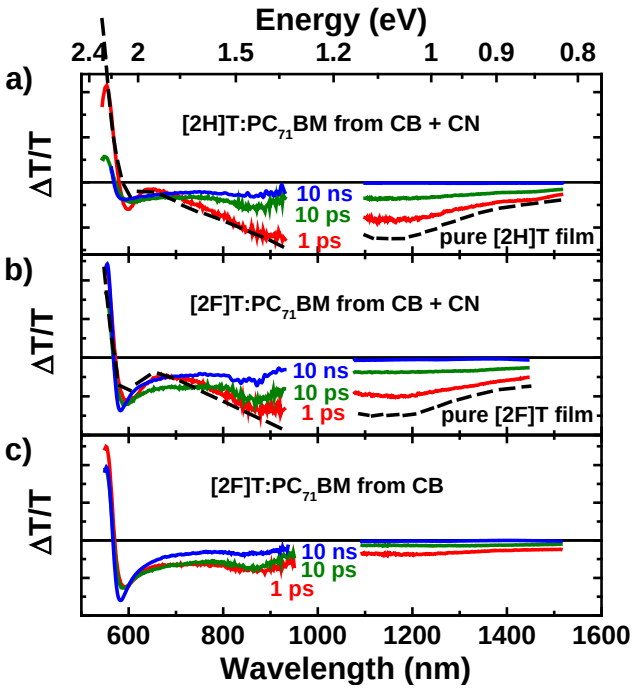

Figure 4. TA spectra of [2X]T:$PC_{71}BM$ prepared with and without CN additives; films excited at 532 nm with 10-11μJ cm^{-2} $pulse^{-1}$. The dashed lines correspond to the exciton-induced absorption spectrum observed at 0.5-0.6 ps on neat polymer films.

A first qualitative assessment of the TA spectra enables us to identify the relevant states and evaluate global trends. **Figure 4** depicts selected TA spectra at time delays of 1 ps, 10 ps, and 10 ns, corresponding to time points at which we expect to monitor the primary photogenerated states (excitons), the charge generation process, and the products (charges) remaining after

exciton decay and charge transfer are completed. The distinctive spectral signatures of excitons and charges are independently determined from TA experiments on neat [2X]T films at short delay times (dashed lines in Figure 4) and on polymer:fullerene blends at intermediate delays (spectra at 10 ns in Figure 4), respectively. In contrast to many other material systems studied recently,[6] no further spectral shift of the photoinduced absorption at longer times that could indicate triplet exciton formation is observed in [2X]T:$PC_{71}BM$ blends.

The TA spectra show two very distinct evolutions in [2H]T:$PC_{71}BM$ films prepared with CN and in [2F]T:$PC_{71}BM$ films prepared without CN, while the blend performing best in solar cells, namely [2F]T:$PC_{71}BM$ films prepared with CN, shows photophysical characteristics in between the two extremes, suggesting a trade-off exists in fully optimized devices. More precisely, [2H]T:$PC_{71}BM$ films prepared with CN (Figure 4(a)) exhibit a strong excitonic signature at 1 ps delay time, with the spectrum being nearly identical to that of neat [2H]T films. Successively, the spectrum evolves into that of the charge-induced absorption, characterized by a broad ‘trapezoidal’ spectral shape with local maxima at 575 and 900 nm and no absorption beyond 1000 nm. In contrast, [2F]T:$PC_{71}BM$ films prepared without CN (Figure 4(c)) instantaneously exhibit pronounced charge-induced absorption, while the excitonic contribution is almost non-existent. Thereafter, the signal decays without further spectral evolution. This difference implies that two distinct charge generation pathways dominate in

these two systems: diffusion-limited exciton dissociation is the predominant process in [2H]T:$PC_{71}BM$ films processed with CN, while ultrafast (sub-100fs) exciton dissociation prevails in [2F]T:$PC_{71}BM$ films processed without CN. Interestingly, the blend with the best performance in solar cells, namely [2F]T:$PC_{71}BM$ prepared with CN as additive, exhibits characteristics of both: a clear initial signature of excitons, however, not as dominant as in the [2H]T based blend (figure 4(b)), accompanied by a quick rise of the charge-induced absorption after several ps delay time. Hence, at a first glance, it appears that exciton-to-charge conversion is slow in [2H]T-based blends, which seems to not be the case in [2F]T based blends; in contrast, the use of solvent additives appears to reduce the fraction of ultrafast charge generation, the same trend is seen in [2H]T-based blends (see **Figure S2**). This observation is in line with facilitated fullerene aggregation as expected when using chloronaphthalene (CN) as solvent additive,[13,14] effectively reducing the fraction of component intermixing that leads to ultrafast charge generation.

Table 1. Exciton dynamics parameterized by a bi-exponential fit to the TA data at energies below 1.2 eV according to $\Delta T / T_{norm}(t) = A_1 e^{-\frac{t}{\tau_1}} + A_2 e^{-\frac{t}{\tau_2}} + y_0$:

Film	A_1	τ_1	A_2	τ_2	y_0
neat [2H]T	32 %	(27 ± 5) ps	61%	(257 ± 6) ps	2.7%
neat [2F]T	20 %	(66 ± 5) ps	69 %	(687 ± 19) ps	6.5%

[2H]T:C71 from CB	37 %	(4.3 ± 0.2) ps	54 %	(50 ± 2) ps	6.3%
[2H]T:C71 from CB + CN	31 %	(2.8 ± 0.2) ps	58 %	(52 ± 2) ps	7.7 %
[2F]T:C71 from CB	59 %	(2.4 ± 0.1) ps	28 %	(28 ± 2) ps	13 %
[2F]T:C71 from CB + CN	58 %	(1.8 ± 0.5) ps	31 %	(28 ± 1) ps	9.4%

The exciton decay time can be readily assessed from the near-infrared spectral region at energies below 1.2 eV, where charge-induced absorption of the polymer is negligible (see Figure 4) and exciton-induced absorption dominates the TA spectra. Parametrized by a bi-exponential function (**Table 1**), the exciton decay shows two important trends: firstly, it is slower in [2H]T-based blends than in [2F]T-based ones. We note that the intrinsic recombination of excitons in neat [2H]T polymer films is faster than in [2F]T polymer films. This, in turn, may lead to additional losses during the charge generation process in [2H]T-based films, as excitons are more likely to recombine prior to dissociating at the donor-acceptor interface. Secondly, exciton decay is virtually unaffected by the use of solvent additives during film preparation. This suggests that the mixed domains, whose total contribution is reduced by the use of CN, are most likely fullerene-rich regions, while the polymer-rich domains are already rather pure even without the use of CN, as indicated by the negligible change of polymer exciton lifetime upon using CN.

A first qualitative comparison of the efficiency of the two charge generation channels can be obtained from the evolution of the ground state bleach of the polymer observed between 540

and 570 nm, which is an approximate measure for the total density of excited states. Clearly, the aforementioned spectral evolution observed in [2H]T:$PC_{71}BM$ films is accompanied by a fast decrease of the ground state bleach within the first 10 ps indicating that a significant fraction of the excitations recombine quickly to the ground state. In contrast, only a small decrease of the ground state bleach is observed in [2F]T:$PC_{71}BM$ films prepared without solvent additives and virtually no decay is seen within the same time range in optimized [2F]T:$PC_{71}BM$ blends prepared with CN, in agreement with the higher short-circuit currents obtained from devices made with the latter. However, the contributions of excitons and charges to the total signal must be disentangled in order to evaluate the charge generation.

2.3.2. Extraction of charge carrier dynamics

To analyze the charge carrier concentration dynamics, denoted here as $A_{charge}(t)$, we need to separate their contribution to the TA data from that of excitons, as the exciton-induced absorption covers the entire spectral range, thus leaving no spectral window to specifically probe the charge carrier dynamics. With the exciton and charge-induced absorption spectra known, this deconvolution is done by solving the following equation for each pump-probe time delay *t*:

$$\Delta T/T(t) = A_{exciton}(t) * S_{\text{exciton}} + A_{charge}(t) * S_{charge} \quad (2)$$

The normalized exciton reference spectrum $S_{exciton}$ is extracted from the TA spectra obtained from neat polymer films that were averaged across delay times between 10 ps and 100 ps, while S_{charge} is extracted from the TA spectra of [2X]T:$PC_{71}BM$ blends averaged between 10 ns and 500 ns (**Figure S3**). Note that $S_{exciton}$ and S_{charge} are normalized spectra; they do not represent the absorbance of a known quantity of excitons or charges. As a result the exciton and charge carrier dynamics, namely $A_{exciton}(t)$ and $A_{charge}(t)$ remain unit-less quantities at this stage. We note that even if the reference spectra were experimentally not accessible, the component spectra could be determined together with their dynamics either by rate equations based global analysis,[8,16,17] or by soft modeling analysis tools such as multivariate curve resolution alternating least squares (MCR-ALS).[6,7,18] We note that such approaches also enable to separate the dynamics of charges from those of other states which may be present, for instance long-lived triplet states.

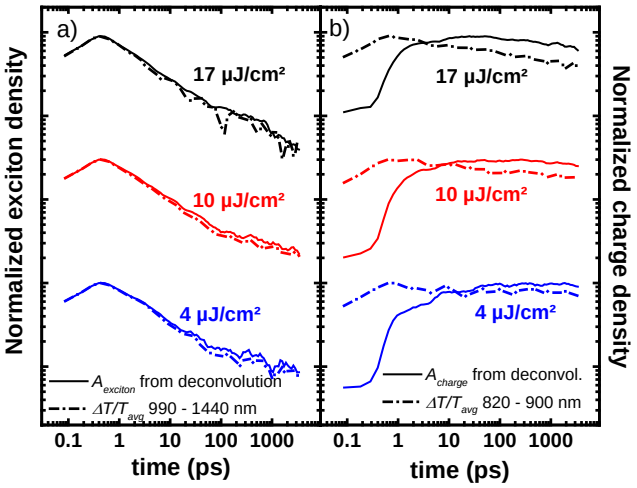

Figure 5. Plots of the sub-ns dynamics of excitons (a) and charges (b) in a [2F]T:$PC_{71}BM$ blend prepared with CN, comparing the kinetics extracted from equation (2) and the decay of the photoinduced absorption in the regions of exciton and charge maximal absorption for various fluences.

For each time delay *t*, $A_{exciton}(t)$ and $A_{charge}(t)$ are scalars, whereas $\Delta T/T$, $S_{exciton}$ and S_{charge} are arrays (*i.e.* one element for each wavelength probed). Consequently, **Equation 2** describes a system of 600 to 700 linear equations for each delay time *t* (one equation for each wavelength) with only two variables $A_{exciton}(t)$ and $A_{charge}(t)$, plus the experimental noise. This redundancy enables averaging, which results in a greatly improved signal-to-noise ratio in comparison to monitoring the kinetics of a given spectral feature only, as shown in **Figure 5** for the [2F]T:$PC_{71}BM$ blend prepared with CN. This improvement is obvious even for excitons (Figure 5(a)), although they can be monitored independently of other excited states in the NIR spectral

region. Moreover, for charges (Figure 5(b)), whose absorption spectrum entirely superimposes that of excitons, deconvolution is the only route to monitor the early time dynamics, and thus the charge generation process.

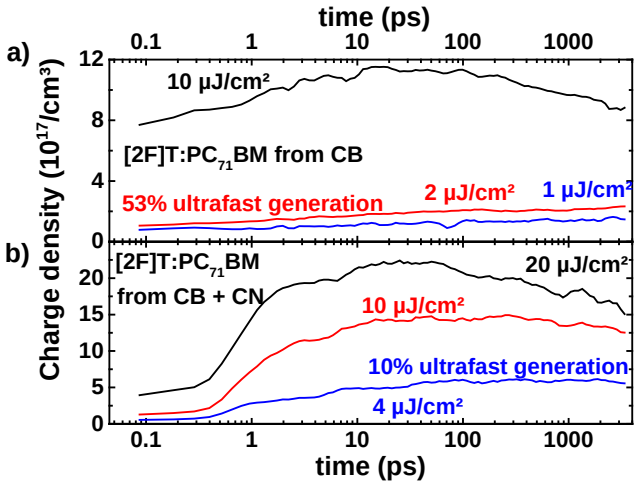

Figure 6. ps-ns charge carrier density dynamics in [2F]T:$PC_{71}BM$ extracted from deconvolution of the TA spectra of films (a) prepared without solvent additives and (b) with 5% CN. The quantification of the charge density is detailed in section 2.3.3.

The extracted unit-less kinetics of the charge carrier concentration $A_{charge}(t)$ confirms the existence of two charge generation channels and also that the use of CN as solvent additive strongly reduces the fraction of ultrafast carrier generation from 53% without additive to 10% with additive in the case of [2F]T:$PC_{71}BM$ blends (see **Figure 6)** and from 33% to 0% for the [2H]T-based blends (**Figure S4**). For the [2F]T:$PC_{71}BM$ film prepared with CN additive, the majority of the carrier population is created up to several tens of ps in line with the exciton

decay, as shown in Table 1. In order to understand which one of these two channels yields the highest photon-to-charge conversion efficiency, we converted the unit-less kinetics into actual densities of charges.

2.3.3.. Quantification of the charge carrier density

In TA spectroscopy the observed change in transmission $\Delta T/T(\lambda)$ caused by one excited state is equivalent to the product of the film thickness d, the density $n(t)$ of absorbing states and the wavelength-dependent absorption cross section $\sigma(\lambda)$, which is not readily accessible, thus impeding quantification:

$$\Delta T/T\,(\lambda) = d \times \sigma(\lambda) \times n(t) \qquad (3)$$

While $\sigma_{exciton}$ can be determined assuming that in a neat polymer film the density of excitons present directly after photoexcitation equals the density of absorbed photons, provided the excitation fluence is low enough to avoid ultrafast non-linear effects such as exciton-exciton annihilation, accessing σ_{charge} is much less straightforward. Guo et al. have previously determined σ_{charge} for P3HT by generating charges in a blend and assuming equal densities of holes in P3HT and of electrons in the acceptor, for which $\sigma_{electron}$ was known.[9] However, countercharges with known σ are a rare exception.[19] Alternatively, one can estimate the density

of charges from the generation efficiency by modeling the recombination losses that are present during the generation time.[10,20] A more direct way has been demonstrated by Durrant and coworkers, who measured $\Delta T/T$ on a device and related it to the integrated short-circuit photocurrent. [21]

Here, we advance this approach by using time-delayed collection field (TDCF) experiments on PBDT[2X]T:$PC_{71}BM$-based devices processed with solvent additives to determine the density of charges and then to compare it to the $\Delta T/T$ measured in TA experiments on films for the same delay. TDCF has recently been used to study the field dependence of charge generation and the carrier recombination dynamics in several organic photovoltaic material systems.[22] The collection field is applied after a fixed delay of 10 ns following pulsed excitation and expedites charge collection thereby minimizing non-geminate recombination, yielding a more accurate estimate of the number of generated charges. To ensure that optical densities measured on films (TA) and charge densities measured on devices (TDCF) were obtained under comparable illumination conditions, we determined the density of absorbed photons in the actual device structure by a transfer matrix formalism using the wavelength dependent refractive index of the blend independently determined by thin film ellipsometry (details in the SI). As depicted in the inset of **Figure 7** the fluence dependence of the charge-induced absorption at 10 ns determined from TA experiments on blend films is in excellent agreement

with the fluence-dependent quantity of charges extracted by TDCF on a photovoltaic device after a delay of 10 ns. Note that, in spite of the collection field, the charge extraction time extends up to one microsecond leaving room for a limited fraction of non-geminate recombination. Thus, our estimate represents a lower boundary for *n*. However, the fluences used here are all below 3 μJ cm^{-2}; non-geminate recombination between 10 ns and 1 μs is typically very small at such low fluences. Note that for other systems, in which non-geminate recombination is observed at earlier times, it is necessary to determine the absorption cross section from only the lowest fluences in order to avoid the recombination of charges during the TDCF extraction pulse and to integrate the optical signal over the whole spectral range which can compensate for the lower signal-to-noise ratio. At present the detection limit of our TA is on the order of excitation fluences around 0.5 μJ cm^{-2} for cross sections in the range of 10^{16} cm^{-2}.

The wavelength dependent cross-section $\sigma(\lambda)$ of charges determined from **Equation 3** using the density of charges as determined from the TDCF experiment for the same density of absorbed photons is shown in Figure 7. The same approach was used for the blends processed without solvent additive, while in this case *n* was estimated from the TDCF results obtained from optimized blends, multiplied by a constant factor accounting for the difference in external quantum efficiency (*EQE*), which is equivalent to the difference in *IQE*, as the absorption of

both blends at 532 nm is virtually identical (see Figure 3). We obtained wavelength dependent absorption cross-sections of charge carriers in the range of 1 – 8 $\times 10^{-16}$ cm^2, well in line with previously reported values for other semiconducting polymers.[10,20,21] The charge-induced absorption spectra of blends prepared with and without CN additive are similar, differing only close to the onset of the ground state bleach, where a much stronger signal is observed for samples processed without CN. In this spectral region, Stark effect signatures can typically be observed, that is, electroabsorption causes a shift of the ground state absorption of chromophores located in the transient electric field created by oppositely charged carriers. In fact, this observation indicates the existence of stronger electric fields and thus a smaller distance between some of the charges across the heterojunction interface in the blends processed without solvent additive. This is consistent with the expected presence of mixed material domains in the blends prepared without CN, where the average distance between countercharges is necessarily limited.

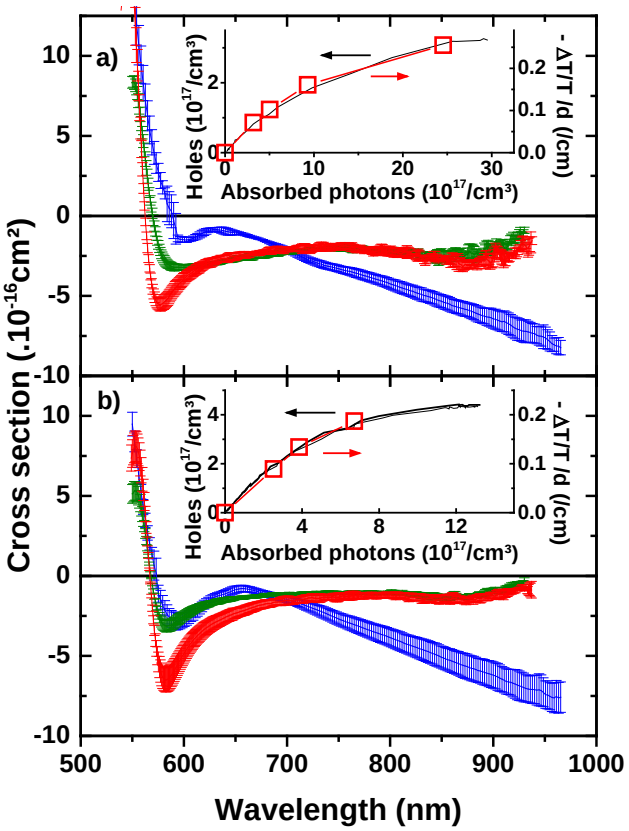

Figure 7. Absorption cross-section $\sigma(\lambda)$ of excitons and charges in (a) [2H]T-based films and (b) [2F]T-based films. Red: charges in [2X]T:$PC_{71}BM$ spincasted from CB, green: charges in [2X]T:$PC_{71}BM$ spin-casted from CB + CN, and blue: singlet excitons in pristine [2X]T films. The error bars represent the standard deviation across cross-sections from different pump fluences. Insets: carrier density extracted from TDCF (black line) as a function of the density of photons absorbed in the active layer of the device, and charge-induced absorption signal - $\Delta T/T/d$ (symbols) from TA signals integrated between 575 nm and 930 nm in [2H]T:$PC_{71}BM$ cast from CB+CN and between 590 nm and 930 nm in [2F]T:$PC_{71}BM$ blends cast from CB+CN, as function of the density of photons absorbed in the film.

From these cross-sections we obtain the densities of charges for all delay times (see Figure 6) and also the yield φ_{CT} of charges generated per absorbed photon. Counterintuitively, but in line with the device performance, we find that in [2F]T-based films, the ultrafast generation observed in the blend prepared without CN, seems to be less efficient than the diffusive generation observed when the films were prepared with solvent additives with a φ_{CT} of 78% in the former and *92%* in the latter, respectively. Here, it appears that in blends processed with additives, fullerene aggregation facilitates fast electron transport and thus efficient separation once the excitons have reached the interface. [16, 23, 24] On the contrary, in the case of [2H]T-based blends, charge generation appears to be rather inefficient independently of the use of processing additives (48% efficiency using additives vs. 51% without additive), which suggests that in [2H]T-based blends the factor that limits dissociation of excitons is their ability to reach the heterojunction rather than to undergo charge transfer at the heterojunction. Interestingly, in the case of [2H]T-based blends, φ_{CT} is much lower than the photoluminescence quenching observed previously.[11] This suggests that excitons arriving at the vicinity of the interface may undergo more non-radiative recombination than in the pure polymer.

2.3.4. Field dependence of charge generation

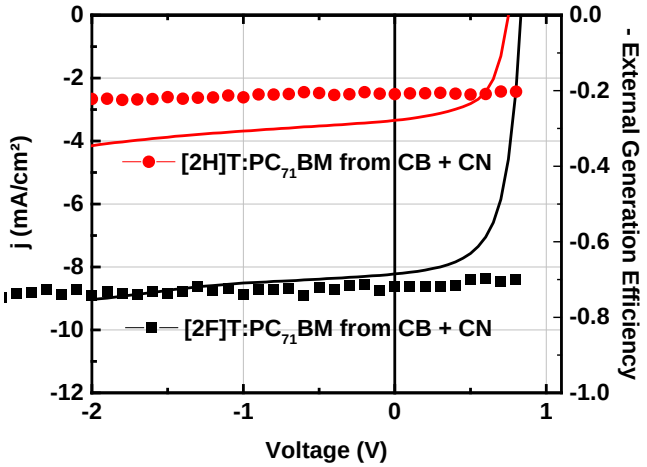

Figure 8. Field dependence of charge generation: J-V curves of [2X]T:$PC_{71}BM$ solar cells processed with CN under white LED illumination (solid lines). External generation efficiency (equivalent to number of charges extracted from TDCF per incident photon) as a function of the prebias applied during the pulsed excitation shown as solid symbols. Note: the low external generation efficiency observed in [2H]T:$PC_{71}BM$ is due to exciton hole annihilation during the pulse width (which is not that case in [2F]T-based devices due to the much shorter exciton lifetime). This effect was not seen in the sub-ns shorter pulse width (120 fs), in turn enabling us to accurately characterize charge generation, while it is present in the ns-µs TA used for determining the charges cross section, thus ensuring compatibility with the TDCF results.

The rather high fill factors obtained from [2X]T-based devices (compare Table S1) suggest that exciton dissociation into spatially-separated charges is not only an exergonic process, but also occurs barrier-less. This is confirmed by prebias-dependent TDCF experiments on optimized [2X]T:$PC_{71}BM$ devices. As demonstrated in **Figure 8**, generation of charges is virtually field-independent in both material systems. This confirms that the limited charge generation efficiency observed in optimized [2H]T-based blends is not a consequence of a lack

of driving force during dissociation, but rather of oversized polymer domains incompatible with the limited exciton diffusion length leading to exciton recombination prior to reaching the heterojunction. In fact, this is in good agreement with the prolonged exciton decay in [2H]T-based blends compared with the more efficient [2F]T-based blends (see Table 1).

2.4. Charge carrier separation: decay parametrization

Evaluating the next step of charge generation, the separation of charges, requires distinguishing between charges that remain at the interface in bound charge pairs (BCP) and those that are entirely separated, namely spatially-separated charges (SSC). Our previous work has demonstrated that the experimentally observed decay of the population of charges can often be described by considering BCP and SSC as two separate pools initially populated by a fraction *(1-f)* and *f*, respectively, of the overall charge density.[10] Results by Bakulin et al. support the existence of two charge carrier pools created after photoexcitation as they showed that a reservoir of charges not participating to photocurrent exists which undergoes a sub ns- to ns decay, analogous to our pool of BCPs, from where they managed to promote charges to the population participating to photocurrent, our SSC pool, by applying an IR (0.5 eV) “push” pulse on a sub-ns timescale. [24]

However, in TA experiments BCP and SSC often exhibit similar spectral features. Nevertheless, their recombination dynamics and fluence dependence differ and can be used to distinguish them. BCPs recombine geminately which leads to a quasi-exponential decay of their population with an inverse rate constant τ, while SSC undergo non-geminate recombination with a rate that, for organic materials, is empirically found to be proportional to $n^{\lambda+1}$ with the order $\lambda+1$ typically in the range between 2 and 3 and a proportionality factor k_λ. As we have previously shown in separate studies, the assumption of concomitant exponential and power law decays of the entire charge carrier population leads to a set of differential equations, which can be analytically solved to give the following expression, that describes how the initial charge density n_0 decays with time: [10]

$$n(t) = (1-f)n_0\left(1-e^{-t/\tau}\right) + (\lambda k_\lambda t + (f n_0)^{-\lambda})^{-1/\lambda} \quad (4)$$

Parameterizing the dynamics of the charge-induced absorption allows extracting the recombination parameters τ, λ and k_λ, in addition to the fraction f of SSC and the fraction $1-f$ of BCP.

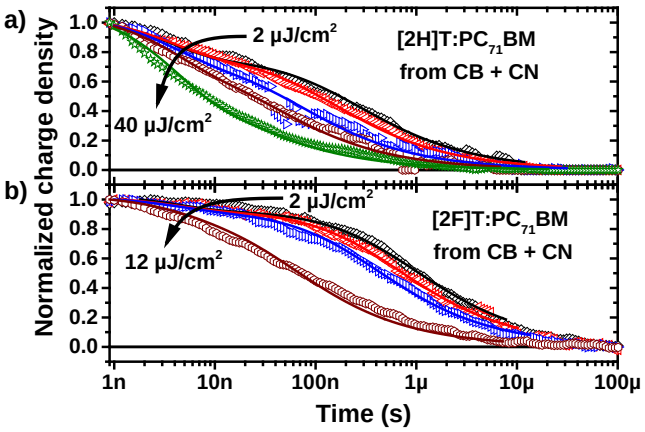

Figure 9. Charge-induced absorption decay dynamics in optimized (a) [2H]T:$PC_{71}BM$ and (b) [2F]T:$PC_{71}BM$ blends (open symbols) and fits of the experimental data to a two-pool model (solid lines). The charge carrier dynamics were obtained from ns-μs transient absorption spectroscopy by averaging the signal across the entire charge-induced absorption spectrum.

As shown in **Figure 9**, **Equation 4** parameterizes the experimentally observed decays of the charge-induced absorption rather well. Here, f, τ, λ and k_λ were used as shared parameters for the entire fluence series, which was then fitted globally with only the initial carrier density n_0 varying from fluence to fluence (more details about the two-pool model characterization, including the specific impact of each parameter on the dynamics, can be found in the SI). All extracted fit parameters are shown in **Table 2** with their variances. The non-geminate recombination coefficient k_λ extracted from the fits is expressed in $(cm^{-3})^{-\lambda}s^{-1}$ and, therefore, its value cannot be readily compared across material systems that have different $\lambda+1$. For a given charge density, we can calculate k_2 which is the equivalent recombination coefficient for a

recombination process that is solely bimolecular ($\lambda = 1$). This coefficient is charge density dependent, as expected from the dispersive character of charge transport in organic materials. We computed the value of k_2 for a charge carrier density of $n_{1SUN} = 5\times10^{15}$ cm^{-3}, typical for OPV devices under one sun illumination conditions (AM 1.5G).[10, 25]

Table 2. Recombination parameters extracted from the global fit of the fluence-dependent charge-induced absorption decay to a two-pool model (equation 4) for [2X]T:$PC_{71}BM$ with (Figure 8) and without (Figure S4) CN additive. For comparison, the previously determined parameters for RR-P3HT:$PC_{61}BM$ are shown as well (Ref. [10]).

Blend	f	τ [ns]	$\lambda + 1$	k_2 [cm^{3}s^{-1}]	$k_2/k_{langevin}$
[2H]T:C71 from CB:	0.9 ± 0.05	1.1 ± 0.2	3 ± 0.01	3.1 ± 0.7×10^{-12}	n/a
[2H]T:C71 from CB + CN	0.77 ± 0.01	3.0 ± 0.2	2.58 ± 0.01	6.4 ± 2×10^{-12}	0.018
[2F]T:C71 from CB	0.91 ± 0.01	2.5 ± 0.3	2.77 ± 0.01	5.9 ± 1×10^{-13}	n/a
[2F]T:C71 from CB + CN	0.93 ± 0.01	4.1 ± 0.6	2.62 ± 0.01	4.9 ± 0.9×10^{-13}	0.0012
RR-P3HT:$PC_{61}BM$ [10]	0.85 ± 0.01	4 ± 0.4	2.45	1.2 ± 0.02×10^{-13}	0.0002

The results obtained from the two-pool model demonstrate that the optimized [2H]T-based blend exhibits a fraction $1-f$ of geminate charge recombination as high as 23%. In contrast, [2F]T-based blends exhibit outstanding charge separation characteristics, even surpassing the ubiquitous RR-P3HT:$PC_{61}BM$ reference system with < 10% of charges lost by geminate recombination. Furthermore, in both material systems, the use of solvent additives is found to decrease the apparent reaction order $\lambda + 1$ of non-geminate recombination, bringing it closer to the order of 2 predicted by Langevin theory. This deviation from Langevin theory is widely

observed in organic semiconductors and has previously been ascribed to the influence of shallow energetic trapping that immobilizes a fraction of the charges thus withholding them from recombination.[20] The lower recombination order obtained from the films processed with additives is thus consistent with the hypothesis of an additive-induced demixing of the two materials, in turn leading to a reduction of the disorder and, as a result, a reduction in the density of shallow energetic traps in this system.

2.5. Charge extraction: extrapolation to device-relevant conditions

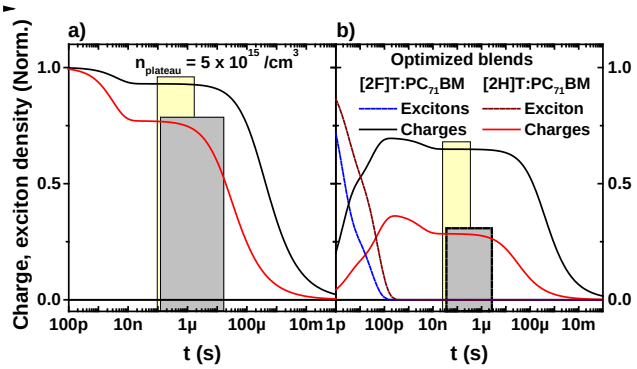

Figure 10. (a) Time-dependent charge carrier densities in optimized [2X]T:PC_{71}BM blends calculated with an initial density of charges prior to non-geminate recombination of 5×10^{15} cm^{-3}, as typically present under 1 sun conditions. (b) Representation of the time-dependent exciton and charge carrier concentrations considering the experimentally-determined charge generation efficiency φ_{CT} (for 532 nm illumination). The rectangles denote the range of extraction times (see SI) estimated for short-circuit conditions in [2F]T:PC_{71}BM (yellow full) and [2H]T:PC_{71}BM (gray dashed) devices of optimal thicknesses, respectively. The exciton decay is modeled by a biexponential decay using the experimentally-determined time constants (Table

1). The same time constants are used for charge generation and the amplitude of the exciton density is normalized to the charge density as given by φ_{CT}.

With the recombination parameters on hand, we are now able to extrapolate equation 4 to other illumination conditions, specifically other values of n_0 such as $n_0 = 5\times10^{15}$ cm^{-3} typical for device operation under 1 sun illumination and, thereby, to reproduce the effects of recombination on device performance. Furthermore, taking into account the difference in the generation efficiency of charges in [2F]T-based and [2H]T-based blends (**Figure 10**), we see that in the time range extending from the maximum extraction time of electrons and the maximum extraction time of holes (rectangles in Figure 10, see calculation in the SI), the density of charges in optimized [2F]T:$PC_{71}BM$ devices is twice that of optimized [2H]T:$PC_{71}BM$ devices, in excellent agreement with the ratio of short-circuit currents measured from actual optimized devices (see Table S1).

Table 3. Quantum efficiencies of the subsequent steps of the photocurrent generation mechanism for an excitation wavelength of 532 nm.

Blend	φ_{abs}[a)]	φ_{CT}[b)]	φ_{sep}[c)]	φ_{extr}[d)]	EQE[e)]	$\varphi_{abs}\times\varphi_{CT}\times\varphi_{sep}$
[2H]T:C71 from CB:	70%	51%	90%	n/a	29%	32%
[2H]T:C71 from CB + CN	77%	48%	77%	68.3 – 99.6%	33%	28%
[2F]T:C71 from CB	72%	78%	91%	n/a	61%	51%
[2F]T:C71 from CB + CN	75%	92%	93%	99.6 – 100%	73%	64%
P3HT:PCBM	82%	n/a	85%[10]	99.2 – 100%	70%	< 64%

a) At 532 nm for optimized active layer thickness obtained from transfer matrix simulation (see SI) for a device structure SiO_2/ITO/PEDOT:PSS/[2F]T:$PC_{71}BM$/Ca/Al with thicknesses 34

0/110/35/Opt/7/100(nm). b) Determined at the maximum charge density. c) *f* as determined from two-pool model, see Table 2. d) Fraction of charges not recombining before the extraction time (see Figure 10) for a charge density prior to non-geminate recombination of 5×10^{15} cm^{-3} which is in the typical operating range of OPV devices under solar illumination. The lower value corresponds to the extraction time of holes and the upper value to the extraction time of electrons. e) EQE at 532 nm from Ref. [11] (blends with additives) and Figure S7 (blends without additives).

The extracted quantum efficiencies of all photophysical processes involved in the photocurrent generation in [2X]T-based solar cells are summarized in **Table 3**. Here, the absorption efficiency φ_{abs} at 532 nm was determined by transfer matrix simulations using optical indexes determined by ellipsometry and for optimal active layer thicknesses (**Figure S8**). Furthermore, the exciton dissociation efficiency φ_{CT} was obtained from the ratio of the maximum density of charges, as determined from TA and TDCF experiments, divided by the density of absorbed photons (see section 2.5), while the charge separation yield φ_{sep} is equivalent to the fraction *f* of spatially-separated charges determined from the two-pool model parameterization of the fluence-dependent charge-induced absorption dynamics. Finally, the extraction efficiency φ_{extr} is the fraction of charges that has not recombined prior to the extraction time, that is, if losses related to extraction barriers are neglected. Here, the extraction time was estimated conservatively as the time required for charges to drift through the entire bulk of the photoactive layer at short-circuit conditions using to V_{OC}/d where *d* is the active

layer thickness and taking into account their mobilities (**Table S4**). However, the dispersion in mobility, the voltage loss across the PEDOT:PSS layer, and offsets between flat band conditions and V_{OC} were neglected.

We note that the product $\varphi_{abs} \times \varphi_{CT} \times \varphi_{sep}$ is in good agreement with the experimentally-determined *EQE* (within 10% deviation). As previously mentioned, TDCF likely underestimates slightly the total number of generated charges, in turn leading to a lower charge generation efficiency $\varphi_{CT,.}$ We note that φ_{extr} should not be taken into account when comparing to the *EQE*, since the *EQE* is typically measured at very low fluences, where non-geminate recombination is negligible.

Clearly, the main positive effects of main-chain fluorine substitution in [2X]T polymers are: (i) the improved exciton dissociation and (ii) the higher charge separation efficiency, both explaining the increased short circuit current. The larger fill factor obtained from [2F]T-based blends is a direct consequence of the lower non-geminate recombination losses (see φ_{extr}), while charge generation is found to be field independent. Additionally, the use of solvent additives further promotes exciton dissociation in [2F]T-based blends compared with "as-cast" blends. In fact, each step following photon absorption in the photocurrent generation cascade exhibits higher efficiency than observed for the reference system RR-P3HT:$PC_{61}BM$. Ultimately, the quantum efficiency of optimized [2F]T:$PC_{71}BM$ blends remains only limited by incomplete

thin-film photon absorption, which cannot be simply increased as an efficiency trade-off occurs between non-geminate recombination (increasing with film thickness) and efficiency of absorption. The trade-off usually arises from charge carrier mobility limitations causing non-geminate recombination of free charges to compete with charge extraction in thicker photoactive layer devices.

2.6. Energetic cost of charge generation

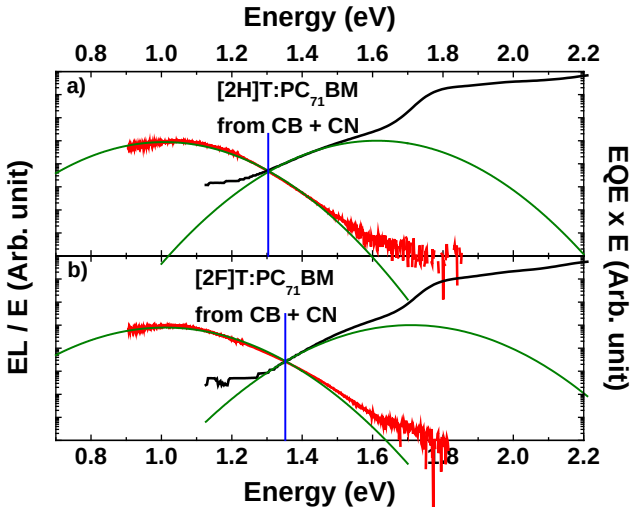

Figure 11. Normalized electroluminescence (left axis, left lines) and EQE (right axis, black lines) reduced spectra for optimized [2H]T:$PC_{71}BM$ and [2F]T:$PC_{71}BM$-based devices. The CT-state energy was determined from the intersection of the normalized Gaussian fits of CT-state absorption and emission according to references [26, 28].

The photocurrent generation process in organic semiconductors is typically associated with an energetic cost. The reference system RR-P3HT:$PC_{61}BM$ exhibits excellent charge carrier generation efficiency (see Table 3), however, even for the lowest energy photons of 1.8 eV absorbed in RR-P3HT:$PC_{61}BM$, two thirds of the photon energy is lost during the photocurrent generation process (resulting in a low V_{OC} = 0.6 V). This is largely a consequence of the offset between energy levels of RR-P3HT and $PC_{61}BM$, which yields a charge transfer state energy as low as 1.1 eV.[26] In contrast, [2X]T polymers exhibit lower HOMO energies than P3HT.[11] As determined by sensitive EQE and electroluminescence (EL) spectroscopy (**Figure 11**) on [2X]T:$PC_{71}BM$ solar cells, a higher energy CT-state of 1.31 eV is observed for optimized [2H]T:$PC_{71}BM$ solar cells and 1.36 eV for optimized [2F]T:$PC_{71}BM$ solar cells. This, in turn, reduces the energetic loss by 33% compared to annealed RR-P3HT:$PC_{61}BM$ solar cells, considering an absorption onset of photons of 1.8 eV. We note that the energy difference of 0.55 eV between E_{CT} and V_{OC} observed for optimized [2F]T:$PC_{71}BM$ blends is in the range typically observed for fullerene-based BHJ solar cells.[27]

3. Conclusions

Correlating results from Vis-NIR transient absorption spectroscopy and time-delayed collection field experiments using a careful evaluation of photon absorption assessed by a

transfer matrix formalism, we showed that the yield of each step in the photocurrent generation in polymer:fullerene BHJ solar cells – here, employing PBDT[2X]T polymers for the case study – can be effectively determined. Deconvolution of the contributions of excitons and charges to the TA spectra allowed us to monitor their individual dynamics. Comparing the TA signal amplitude to the total number of charges extracted in a TDCF experiment under equal excitation conditions, we were ultimately able to determine the absolute charge carrier densities and thus to quantify the exciton dissociation and charge transfer efficiency. Furthermore, coulombically bound charges could be distinguished from spatially-separated charges by their distinct dynamics and fluence dependence using a two-pool parameterization of the charge-induced absorption decay. Following this analytical protocol, we showed that the efficiency of charge separation can be quantified, along with the non-geminate recombination losses obtained by extrapolating the extracted parameters to an excitation density equivalent to 1 sun illumination.

In the specific case study of fluorinated vs. non-fluorinated PBDT[2X]T:$PC_{71}BM$ blends discussed throughout this contribution, we have demonstrated that the higher short-circuit current obtained from fluorinated polymers originates from a ca. 40% higher charge generation yield due to improved exciton diffusion to the heterojunction as evidenced by a faster exciton decay, in conjunction with more efficient charge separation and reduced geminate recombination losses. Furthermore, photocurrent was generated efficiently in [2F]T-based

blends at an even lower energetic cost as a consequence of a 50 meV higher CT-state energy compared to the [2H]T-based blends. The use of solvent additives in [2F]T-based blends was found to further improve the short-circuit current via an increase in charge generation efficiency from 78 % to 92 %. Observing less ultrafast charge generation when using solvent additives while not shortening the exciton lifetime, we conclude that additives mostly increased the purity of fullerene-rich domains. We thus ascribed the improved generation efficiency of blends processed with additives to improved electron transport from the interface in turn enhancing charge separation. Consistent with the decrease in donor-acceptor intermixing and thus energetic disorder, the effective reaction order of the recombination of separated charges became smaller. Overall, the photocurrent generation efficiency in PBDT[2F]T:$PC_{71}BM$-based BHJ solar cells was found to be as good as that of the benchmark RR-P3HT:$PC_{61}BM$ (once thermally annealed), as an increased charge dissociation efficiency outweighed the slightly lower absorption of the former. In fact, the photon absorption limitations linked to the modest carrier mobilities in polymer:fullerene blends remain an issue to be addressed in future material development: here, those parameters set a limit on the maximum photoactive layer thickness achievable without notably increasing the fraction of non-geminate recombination losses. Nevertheless, PBDT[2F]T:$PC_{71}BM$-based BHJ solar cells clearly outperform the RR-P3HT:$PC_{61}BM$ as photoactive material, as similar photogeneration efficiencies could be

obtained with 33 % less energy loss due to the higher CT-state energy in [2F]T-based solar cells.

The methodology described herein allowed the yield of each step of the photocurrent generation mechanism to be determined, ultimately not only enabling to relate structural modifications and film processing conditions to the overall device performance, but also to subtle changes of the individual photophysical processes and their specific efficiency. This yields precise insights into the interplay of chemical structure and material processing and the way to maximize the efficiency of each of those steps overall leading to better device performance. This is of utmost importance for the evaluation of new materials systems at a time where many new donor-acceptor combinations – based on nonfullerene acceptors – are developed, which exhibit new and exciting photophysical properties to be studied in future work.

4. Experimental Section

Transient Absorption Spectroscopy: Transient absorption (TA) measurements were performed with a home-built pump-probe setup. The output of a commercial titanium:sapphire amplifier (Coherent LIBRA HE, 3.5 mJ, 1 kHz, 100 fs) was split into two beams that independently pumped two optical parametric amplifiers (Coherent OPerA Solo). One optical parametric amplifier (OPA) was used to generate the excitation pulses in the visible, while the second OPA was used to generate the seed beam for white-light generation. For measurements in the spectral range between 550-1100 nm, a 1300 nm seed was focused into a c-cut 3 mm thick sapphire window for white-light generation. The variable delay of up to 4 ns between pump and probe was introduced by a broadband retroreflector mounted on a mechanical delay stage. The excitation pulse was chopped at 500 Hz, while the white-light pulses were dispersed onto a linear silicon photodiode array, which was read out at 1 kHz. Adjacent diode readings corresponding to the transmission of the sample after an excitation pulse and without an excitation pulse were used to calculate $\Delta T/T$.

For measurements in the time range between 1 ns to 1 ms with a resolution of 600 ps, the excitation pulse was provided by an actively Q-switched Nd:YVO_4 laser (AOT Ltd. MOPA) at 532 nm. The delay between pump and probe in this case was controlled by an electronic delay

generator (Stanford Research Systems DG535). TA measurements were performed at room temperature under a dynamic vacuum of $<10^{-5}$ mbar.

For TA measurements in the NIR spectral range covering 1100 - 2000 nm a 2100 nm seed was used to generate white-light, a dichroic mirror was used to separate the residual idler beam (2100 nm) from the white-light supercontinuum. The NIR white-light pulses were dispersed onto a Peltier-cooled 512 pixel long linear extended InGaAs array (Entwicklungsbüro Stresing) and read out as described above.

UV-Vis Absorption Spectroscopy: Steady state absorption spectra were measured with a Perkin Elmer Lambda 25 spectrometer. The layer thickness was determined with a Tencor P10 surface profilometer.

Time-delayed Collection Field. Devices were prepared according to the protocol described by Wolf et al.[11] In all TDCF experiments, charges were generated with laser pulses from a commercial Nd:YAG laser pumping an optical parametric oscillator (NT242 EKSPLA, 5.5 ns pulse width, 500 Hz repetition rate, 532 nm excitation wavelength). After a delay time of 10 nanoseconds, an extraction reverse voltage of -4V was applied with a pulse generator (Agilent 81150A). The resulting current was measured with a Yokogawa DL9140 oscilloscope via a 50 Ω input resistor. The total photogenerated charge Q_{tot} was obtained by integration of the current transient until 1 µs. Small diode area (1 mm²) was used in order to reduce the *RC* response time.

For fluence-dependent generation experiment, the sample was excited at a voltage close to open circuit voltage, in order to avoid contributions from field-assisted charge generation, which are absent in TAS experiments. For field-dependent generation, a prebias was applied during the excitation pulse and varied between -2 and 0.8V. The extraction voltage of -4V was applied after 10 ns to prevent non–geminate recombination during extraction.

External quantum efficiency (EQE): EQE measurements were performed at zero bias by illuminating the device with monochromatic light supplied from a Xenon arc lamp in combination with a dual-grating monochromator. The number of photons incident on the sample was calculated for each wavelength by using a silicon photodiode calibrated by NIST. The *EQE* setup is installed inside a glove box with a controlled nitrogen environment.

Electroluminescence and high sensitivity EQE: For the high-sensitivity *EQE* in Figure 11, the photocurrent was measured under monochromatic illumination (Oriel Cornerstone monochromator in combination with a 200 W halogen lamp) at zero bias, and the calibration of the incident light was performed with a UV enhanced Silicon photodiode (Newport 818-UV) and a Germanium photodiode (Newport 818-IR).

The electroluminescence spectra were acquired with an Andor SR393i-B spectrometer equipped with a silicon detector DU420ABR-DD and an InGaAs DU491A-1.7 detector.

Spectra were collected with both detectors at an injection current comparable to the short circuit current at AM1.5G illumination intensity and normalized.

Supporting Information
Supporting Information is available from the Wiley Online Library or from the author.

Acknowledgements
The research reported in this publication was supported by funding from King Abdullah University of Science and Technology (KAUST).

Received: ((will be filled in by the editorial staff))
Revised: ((will be filled in by the editorial staff))
Published online: ((will be filled in by the editorial staff))

[1] a) M. A. Green, K. Emery, Y. Hishikawa, W. Warta, E. D. Dunlop, *Prog. Photovolt: Res. Appl.*, **2016**, *24*, 905; b) C. Battaglia, A. Cuevas, S. De Wolf, *Energy Environ. Sci.*, **2016**, *9*, 1552

[2] M. M. Lee, J. Teuscher, T. Miyasaka, T. N. Murakami, H. J. Snaith, *Science*, **2012**, *338* (6107), 643

[3] a) W. S. Yang, J. H. Noh, N. J. Jeon, Y. C. Kim, S. Ryu, J. Seo, S. I. Seok, *Science*, **2015**, *348* (6240), 1234; b) M. Saliba, T. Matsui, J.-Y. Seo, K. Domanski, J.-P. Correa-Baena, M. K. Nazeeruddin, S. M. Zakeeruddin, W. Tress, A. Abate, A. Hagfeldt, M. Grätzel, *Energy Environ. Sci.*, **2016**, *9*, 1989

[4] S. Li, L. Ye, W. Zhao, S. Zhang, S. Mukherjee, H. Ade, J. Hou, *Adv. Mater*., **2016**, *28*, 9423

[5] M. C. Scharber, N. S. Sariciftci, *Prog. Polym. Sci.*, **2013**, *38* (12), 1929-1940.

[6] a) J. R. Ochsmann, D. Chandran, D. W. Gehrig, H. Anwar., P. K. Madathil, K.-S. Lee, F. Laquai, *Macromol. Rapid Commun*. **2015**, *36*, 1122; b) F. Etzold, I. A. Howard, N. Forler, A. Melnyk, D. Andrienko, M. R. Hansen, F. Laquai, *Energy Environ. Sci*. **2015**, *8*, 1511

[7] a) C. Dyer-Smith, I. A. Howard, C. Cabanetos, A. El Labban, P. M. Beaujuge, F. Laquai, *Adv. Energy Mater.*, **2015**, *5*, 1401778; b) A. K. K. Kyaw, D. Gehrig, J. Zhang, Y. Huang, G. C. Bazan, F. Laquai, T.-Q. Nguyen, *J. Mater. Chem. A*, **2015**, *3*, 1530; c) D. W. Gehrig, S. Roland, I. A. Howard, V. Kamm, H. Mangold, D. Neher, F. Laquai, *J. Phys. Chem. C*, **2014**, *118* (35), 20077; d) K. D. Deshmukh, S. K. K. Prasad, N. Chandrasekaran, A. C. Y. Liu, E. Gann, L. Thomsen, D. Kabra, J. M. Hodgkiss, C. R. McNeill, *Chem. Mater.*, **2017**, *29* (2), 804.

[8] a) S. Karuthedath, T. Sauermann, H.-J. Egelhaaf, R. Wannemacher, C. J. Brabec, L. Lüer, *J. Mater. Chem. A*, **2015**, *3*, 3399; b) L. Lüer, V. Moulisová, S. Henry, D. Polli, T. H. P. Brotosudarmo, S. Hoseinkhani, D. Brida, G. Lanzani, G. Cerullo, R. J. Cogdell, *Proc. Natl. Acad. Sci. USA*, **2011**, *109* (5), 1473

[9] J. Guo, H. Ohkita, S. Yokoya, H. Benten, S. Ito, *J. Am. Chem. Soc.*, **2010**, *132* (28), 9631.

[10] I. A. Howard, R. Mauer, M. Meister, F. Laquai, *J. Am. Chem. Soc.*, **2010**, *132*, 14866.

[11] J. Wolf, F. Cruciani, A. El Labban, P. M. Beaujuge, *Chem. Mater.*, **2015**, *27* (12), 4184.

[12] K. Do, Q. Saleem, M. K. Ravva, F. Cruciani, Z. Kan, J. Wolf, M. R. Hansen, P. M. Beaujuge, J.-L. Brédas, *Adv. Mater.*, **2016**, *28*, 8197.

[13] X Fan, J. Wang, H. Huang, H. Wang, *ACS Photonics*, **2014**, *1* (12), 1278

[14] M. Abdelsamie, A. El Labban, R. Munir, Z. Kan, S. Dey, D. Anjum, D.-M. Smilgies, P. M Beaujuge, A. Amassian, Polymer-fullerene bulk-heterojunction solar cells: Role of solvent additives in fullerene aggregation, *in preparation*.

[15] C. Schwarz, F. Milan, T. Hahn, M. Reichenberger, S. Kümmel, A. Köhler, *Adv. Funct. Mater.*, **2014**, *24*, 6439.

[16] S. Gélinas, A. Rao, A. Kumar, S. L. Smith, A. W. Chin, J. Clark, T. S. van der Poll, G. C. Bazan, R. H. Friend, *Science*, **2014**, *343*, 512.

[17] L. J. G. W. van Wilderen, C. N. Lincoln, J. J. van Thor, *PLoS ONE*, **2011**, *6* (3), e17373.

[18] a) J. Jaumot, R. Gargallo, A. de Juan, R. Tauler, *Chemometr. Intell. Lab.*, **2005**, *76* (1), 101; b) I. A. Howard, H. Mangold, F. Etzold, D. Gehrig, F. Laquai, in *Ultrafast Dynamics in Molecules, Nanostructures and Interfaces*, Vol. 8 (Eds: H. G. Gurzadyan, G. Lanzani, C. Soci, T. C. Sum), World scientific, Singapore, **2014**, Ch. 4.

[19] For example Guo et al. had to use two steps, first determining the σ of anions in a Silicon phtalocyanine (SiPC) from a blend with a phenylenediamine derivative whose cation σ was known, and then blending this SiPC with P3HT to know the absorption σ of P3HT cations.

[20] J. Gorenflot, M. C. Heiber, A. Baumann, J. Lorrmann, M. Gunz, A. Kämpgen, V. Dyakonov, C. Deibel, *J. Appl. Phys*, **2014**, *115*, 144502.

[21] a) C. G. Shuttle, B. O'Regan, A. M. Ballantyne, J. Nelson, D. D. C. Bradley, J. R. Durrant, *Phys. Rev. B*, **2008**, *78*, 113201. b) T. M. Clarke, F. C. Jamieson, J. R. Durrant, J. *Phys. Chem. C*, **2009**, *113* (49), 20934

[22] a) T. Offermans, S. C. J. Meskers, R. A. J. Janssen, *J. Appl. Phys.*, **2006**, *100* (7), 74509; b) S. Albrecht, W. Schindler, J. Kurpiers, J. Kniepert, J.C. Blakesley, I. Dumsch, S. Allard, K. Fostiropoulos, U. Scherf, D. Neher, *J. Phys. Chem. Lett.*, **2012**, *3*, 640; c) M. Mingebach, S. Walter, V. Dyakonov, C. Deibel, *Appl. Phys. Lett.*, **2012**, *100* (19), 193302; d) D.W. Gehrig, S. Roland, I.A. Howard, V. Kamm, H. Mangold, D. Neher, F. Laquai, *J. Phys. Chem. C*, **2014**, *118*, 20077; e) A. Zusan, B. Gieseking, M. Zerson, V. Dyakonov, R. Magerle, C. Deibel, *Sci. Rep.*, **2015**, *5*, 8286; f) J. Kurpiers, D. Neher, *Sci. Rep.*, **2016**, *6*, 26832.

[23] a) H. M. Feier, O. G. Reid, N. A. Pace, J. Park, J. J. Bergkamp, A. Sellinger, D. Gust, G. Rumbles, *Adv. Energy Mater*., **2016**, *6*, 1502176; b) G. D'Avino, S. Mothy, L. Muccioli, C.

Zannoni, L. Wang, J. Cornil, D. Beljonne, F. Castet, *J. Phys. Chem. C*, **2013**, *117*, 12981, c) H. Tamura, I. Burghardt, *J. Am. Chem. Soc.*, **2013**, *135*, 16364.

[24] A. A. Bakulin, A. Rao, V. G. Pavelyev, P. H. M. van Loosdrecht, M. S. Pshenichnikov, D. Niedzialek, J. Cornil, D. Beljonne, R. H. Friend, *Science*, **2012**, *335*, 1340.

[25] F. Etzold, I. A. Howard, R. Mauer, M. Meister, T.-D. Kim, K.-S. Lee, N. S. Baek, F. Laquai, *J. Am. Chem. Soc.*, **2011**, *133* (24), 9469.

[26] K. Vandewal, K. Tvingstedt, A. Gadisa, O. Inganäs, J. V. Manca, *Phys. Rev. B*, **2010**, *81*, 125204.

[27] K. Vandewal, *Annu. Rev. Phys. Chem.*, **2016**, *67*, 113.

[28] a) R. A. Marcus, *J. Phys. Chem.*, 1**989**, *93*, 3078 b) I. R. Gould, D. Noukakis, L. Gomez-Jahn, R. H. Young, J. L. Goodman, S. Farid, *Chem. Phys.*, **1993**, *176*, 439.

Table of content

The individual efficiencies and losses associated with each step of photocurrent generation in PBDT[2X]T:$PC_{71}BM$ solar cells are determined using a combination of advanced transient spectroscopic, charge extraction, and steady-state spectroscopic techniques, aiding the development of a fuller understanding of the complex interplay between chemical structure, thin film processing conditions, and their impact on device performance.

Keyword
Organic photovoltaics

Julien Gorenflot, Andreas Paulke, Fortunato Piersimoni, Jannic Wolf, Zhipeng Kan, Federico Cruciani, Abdulrahman El Labban, Dieter Neher, Pierre M. Beaujuge, Frédéric Laquai**

From Recombination Dynamics to Device Performance: Quantifying the Efficiency of Exciton Dissociation, Charge Separation and Extraction in Bulk Heterojunction Solar Cells with Fluorine-Substituted Polymer Donors

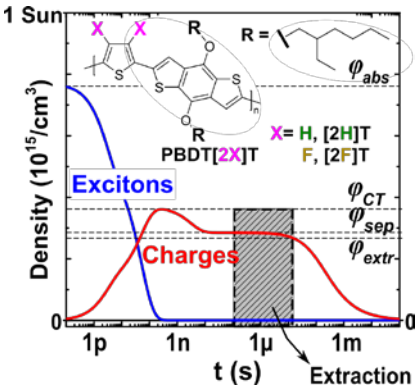
1 Sun
X
X
R
O
S
S
S
O
R
n
R =
φabs
PBDT[2X]T
X= H, [2H]T
F, [2F]T
Excitons
φCT
φsep
φextr
Charges
Density (10^15/cm^3)
0
0
1p
1n
1μ
1m
t (s)
Extraction